Taylor & Francis
Taylor & Francis Group

Materials and Manufacturing Processes

ISSN: (Print) (Online) Journal homepage: https://www.tandfonline.com/loi/lmmp20

Laser fabricated nickel-based coating with different overlap modes

Yu Zhao, Ying Chen, Tianqi Zhang & Tianbiao Yu

To cite this article: Yu Zhao, Ying Chen, Tianqi Zhang & Tianbiao Yu (2021) Laser fabricated nickel-based coating with different overlap modes, Materials and Manufacturing Processes, 36:14, 1618-1630, DOI: 10.1080/10426914.2021.1926490

To link to this article: https://doi.org/10.1080/10426914.2021.1926490

MATERIALS AND MANUFACTURING PROCESSES
2021, VOL. 36, NO. 14, 1618–1630
https://doi.org/10.1080/10426914.2021.1926490

Laser fabricated nickel-based coating with different overlap modes

Yu Zhao, Ying Chen, Tianqi Zhang, and Tianbiao Yu

School of Mechanical Engineering and Automation, Northeastern University, Shenyang, China; Liaoning Provincial Key Laboratory of High-End Equipment Intelligent Design and Manufacturing Technology, Northeastern University, Shenyang, China

ABSTRACT

Ni204 cladding layers were prepared on the surface of 45# steel alloys via laser cladding under different overlap modes. The effects of overlap modes on microstructure evolution, microhardness, wear resistance, compressive and tensile strength were investigated. The intensity of the diffraction peaks is related to the cladding strategy. The remelting mode introduced by "double vertical cross" reduces the cooling rate and improves the uniformity of microstructure, exhibiting a stability of the microhardness and wear resistance. $Cr_{0.19}Fe_{0.7}Ni_{0.11}$, [Fe, Ni], and Ni–Cr–Nb–Mo are primary detected phases in the cladding layer. With the increase in overlap uniformity, the content of [Nb, Mo] which precipitated in grain boundary increases and the microstructure is refined. The uniform microstructure distribution promotes the stable distribution of microhardness and friction coefficient. The angle between the extension direction of the overlap area and the applied loading directly determines the performance of the Ni204 alloy after yielding. The inter-laminar overlap mode weakens the effect of shear stress induced by microstructure differences.

ARTICLE HISTORY
Received 8 December 2020
Accepted 19 April 2021

KEYWORDS
Laser cladding; Ni204 alloy; overlap mode; microstructure; mechanical property

Introduction

Nickel (Ni)-based alloys are the most widely used type of self-fluxing alloy powder[1] owing to its excellent comprehensive performance. For example, good wettability, corrosion resistance, oxidation resistance and good impact toughness.[2] Ni-based alloy has been widely used in many branches of industry as a laser cladding powder, such as automobile, oil and gas, transport and machine tool.[3,4] However, internal defects in laser-cladded components limit their further application. The crack and pore appear in the cladded component, causing hidden risks and short service life. In addition, the inhomogeneity layer performance generated by microstructure cannot be ignored. Therefore, it is important to strengthen the metallurgical bonding zone quality and improve the microstructure homogenize. Several factors, such as cladding parameters, overlap rate, scanning strategy and temperature distribution are primarily responsible for the mechanical properties.[5–7]

Fesharaki et al.[8] prepared the Inconel 625 coating by laser and TIG cladding methods, respectively. Compared with TIG-cladding method, the laser cladding exhibits a higher cooling rate and obtains the coating with a finer microstructure. Qian et al.[9] proved that the density of dislocation has a linear effect on the inhomogeneity of hardness and microstructure of the Ni-based coating using laser cladding. Zeng et al.[3] investigated the effect of laser power on the microstructure and porosity of the Ni-based coating. The results show that the porosity is not a monotonous change with the increasing of laser power. Noteworthy, the cracks are easily produced in the multilayers under cooling shrinkage stress[10] and the uneven microstructure mainly appears in the overlap zone.[11] Li et al.-[12] preheated the substrate before preparing the cladding layers, which reduced the thermal stress and the probability of cracking. Petrat et al.[13] pointed out that the scanning strategy is primarily responsible for the temperature evolution, affecting the temperature gradient and the temperature distribution. The boundary conditions of the cladding layer determine the heat dissipation, which affects the accumulation of heat dissipation.

Over recent years, the research of Ni-based alloy is mainly focused on reducing crack and porosity and improving mechanical properties. The effects of laser cladding scanning strategies on the temperature and performance of coating are widely concerned. Different in-layer scanning modes and interlayer overlap modes generate corresponding temperature distribution,[14,15] affecting its microstructure and performance. Ren et al.[16] proposed a three-dimensional (3D) finite element analysis model to investigate the effect of scanning strategies. For laser cladding of rectangular region, the Zigzag_Y scanning strategy has a lower peak temperature near the cladding track and faster heat dissipation, resulting in a uniform temperature distribution. It also makes residual stress on the Y-axis more uniform and a smaller deformation. Paydas et al.[17] studied the effect of repair strategy on the macrostructure, hardness, microstructure and mechanical properties. The results show that the temperature accumulation and temperature gradient generated by scanning strategy and incident energy directly determine the microstructure characteristics. The overlap rate has a significant effect on the surface roughness of the clad layer and affects the quality of interlayer overlap zone.[18] Callejia et al.[19] fabricated a coating on the semi-spherical surface with the optimal parameters and strategies. The sample with zigzag scanning strategy in layer and perpendicular to each other in adjacent layers has few

CONTACT Tianbiao Yu tianbiaoyudyx@gmail.com School of Mechanical Engineering and Automation, Northeastern University, Shenyang 110819, China

pores and cracks. Although the samples with various scanning strategy observed the pores and cracks, the sample with zigzag scanning strategy in layer and perpendicular to each other in adjacent layers presents a better internal quality. The large thermal stress and residual stress can be reduced by increasing the overlap rate and preheating powder.[20] Petrat et al.[13] pointed out that the scanning strategy has an obvious effect on the temperature evolution. The temperature distribution varies with the scanning strategy, which has been reported in Ren et al.[16] studies. Therefore, the scanning strategy can be considered as an important factor affecting layer performance.

According to the previous studies, the research of scanning strategy mainly focuses on intra-layer, and the overlap mode between the two adjacent layers are usually perpendicular to each other. The defects and uneven microstructure are still observed in the lap joint area of the prepared coating, which affect the performance of the coating. The interlayer overlap mode can improve the temperature distribution, heat dissipation, temperature gradient, grain growth orientation. At present, few literatures have reported the effect of scanning strategy on the Ni204 cladding layer on the surface of 45# die steel. In particular, the effect of interlayer overlap mode on the isotropy of coating properties. This paper studied the influence of such Ni204 layers fabricating by five different scanning strategies on the section morphology, phase composition. In addition, the influence of scanning strategy on the directivity of mechanical properties was also studied.

Materials and methods

Process parameters and cladding system

The 45# die steel with the size of 100 mm × 200 mm × 20 mm was selected as the substrate. The cladding material is the spherical Ni204 alloy powder with sizes ranging from 53 to 150 μm (100–270 mesh). The compositions of 45# die steel and Ni204 alloy powder (supply by Nanjing Institute of Advanced Laser Technology (China)) are given in Table 1. The powder is dried for 6 hours at 80°C before using to avoid the moisture reacting with powder, and also protects the optical circuit system from damage by the oxide smoke.

The open-loop controlled laser cladding system was used in the experiment, wherein YLR-500 optical fiber laser is used to generate a laser beam, laser beam quality is 8 mm·mrad, beam wavelength is 1020 nm, defocusing amount is 0–2 mm. Offline programming software was employed to design and optimize the cladding strategy, as shown in Fig. 1. Cladding trajectory planning mainly includes four parts. First, set TCP value and fix z-axis: define the reference point and ensure the laser head to straight down during its movement. Second, set step distance: ensure the high fitting of the actual motion trajectory

Table 1. Chemical composition (wt%) of 45 steel and Ni204 steel powder (provided by suppliers).

	C	P,S	Si	Cr	Ni	Mn	Mo	Nb	Cu	Fe
Ni204	≤0.03	–	0.4	21	Bal.	–	9	4	–	1.5
45 steel	0.42–0.5	≤0.045	0.17–0.37	≤0.25	≤0.25	0.5–0.8	–	–	≤0.25	Bal.

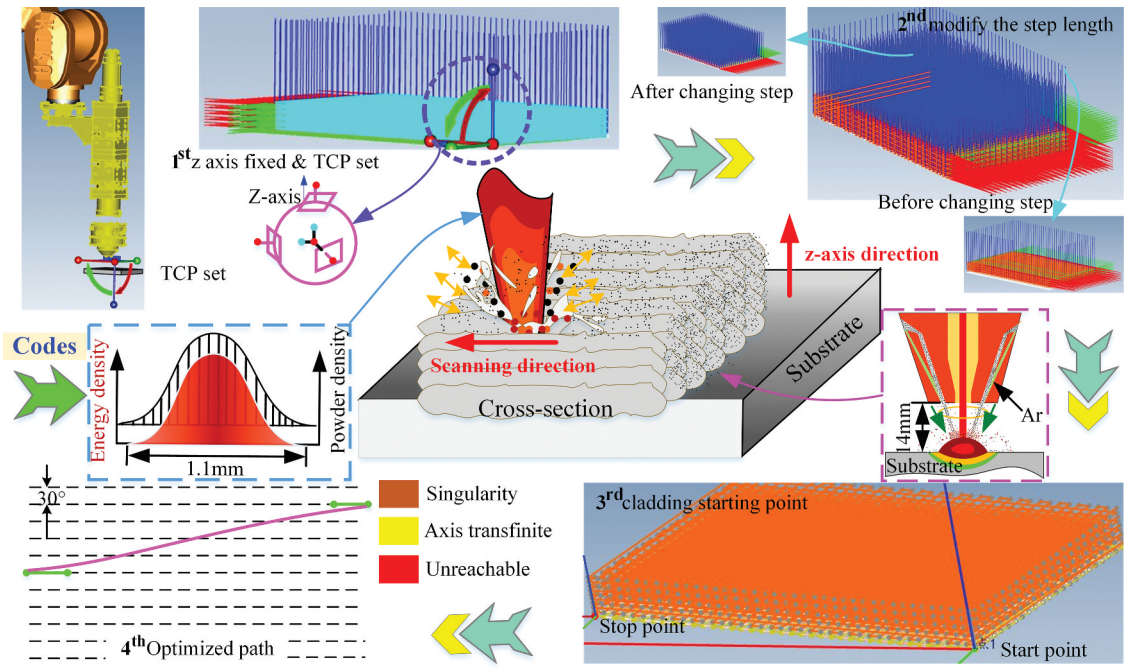

Figure 1. Laser cladding processing.

and the design trajectory. Third, determine the starting and ending positions: uniform distribution of trajectory starting and ending points to improve the quality of the layer boundary. Fourth, optimize the paths: avoid singularities, axis transfinite, and laser head rotation.[14,21] The energy distribution of the laser spot is Gauss distribution, and the powder is transported by coaxial powder feeding system. The focus of the powder beam coincides with the laser beam.

In this study, the transverse overlap rate is 34.8% (the spacing is 0.9 mm) and the longitudinal overlap rate is 42.9% (the spacing is 0.4 mm). The values of shielding gas and powder carrier gas (99.99% argon gas) are 15 l/min and 8 l/min, respectively. Laser power is 450 W, the powder feeding disc rate is 0.7 r/min (11.056 g/min), and the scanning speed is 7 mm/s (The obtained geometric dimensions of the single clad track are: the width is 1.38 mm, the depth is 0.22 mm, and the height is 0.48[22]). The specific experimental parameters are given in Table 2.

Table 2. Optimal operating parameters for multi-layer DLF of N204 alloy powder.

Process parameter	Value	Process parameter	Value
Laser power	450 W	Powder carrier gas	8 L/min
Scanning speed	7 mm/s	Shielding gas	15 L/min
Powder feeding rate	0.7 r/min (11.056 g)	Wavelength of laser	1020 nm
Track spacing	0.9 mm	Spot size of beam	1.1 mm (450 W)
Z axis increasing	0.4 mm		

Process design

The temperature distribution in the cladding layer directly determines the internal microstructure and the performance of the cladding layer. Different overlap modes can generate different remelting modes on the solidification layer, rebuild the direction and position of the metallurgical bonding zone. Therefore, five different overlap modes were designed to study the effects on the properties of Ni204-based alloy, as shown in Fig. 2(a). The five overlap modes are the different combinations of four intra-layer scanning paths (Fig. 2(b)). The mode 1 ('long straight') consists of paths 2. The mode 4 ('short straight') consists of paths 1. The mode 2 ('vertical cross') consists of alternate appear paths 1 and 2. The mode 3 ('oblique vertical cross') consists of alternate appear paths 3 and 4, the angle between the paths and sample boundary is 45°. The one-period trajectory of mode 5 ('double vertical cross') consists of paths 1–4, the angle between the paths 1 and 3 is 45°.

After the cladding, the tensile samples (samples 1–5) were prepared according to the size in Fig. 2(c). The specification for the tensile sample: the thickness is 4 mm, the total length is 105 mm, the chuck length is 25 mm, the parallel length is 30 mm, and the width is 20 mm. Compressive, microhardness and wear samples were prepared in the way shown in Fig. 2(d). The compressive strength samples are Φ5 mm×10 mm cylinders, along the scanning direction is defined as samples 1–1, 2–1, and 5–1, while along the z-axis direction is samples 1–2, 2–2, and 5–2, as shown in Fig. 2(e). The dimension of microhardness and wear samples was prepared along the scanning direction (samples 1–3, 2–3, and 5–3) and z-axis direction (samples 1–4, 2–4, and 5–4) is 10 mm×10 mm×5 mm, as shown in Fig. 2(f).

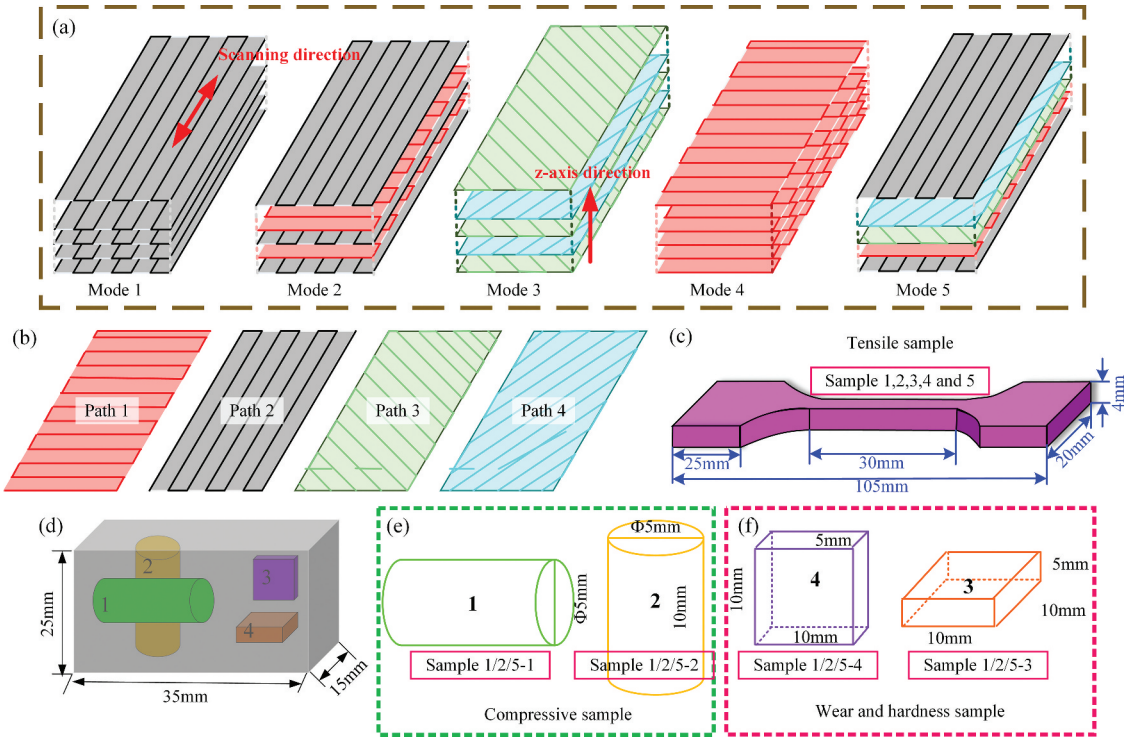

Figure 2. Experiment design. (a) Overlap mode; (b) Intra-layer scanning paths; (c) Tensile samples size; (d) Compressive, microhardness, and wear samples preparation; (e) Compressive samples size; (f) Microhardness and wear samples size.

All prepared samples were ground and polished with different types of sandpaper (240#, 400#, 600#, 800#, 1000#, 1500#, and 2000#) and water-soluble diamond polishing pastes (W2.5 and W0.5). The samples were etched in a 2:1:1 vol HCl: HNO_3: H_2O hybrid solution for 120–150 S to prepare metallographic sample.[22] The laser confocal microscope (LEXTOLS4100) and field emission scanning electron microscopy (SEM, ULTRA PLUS) were used to observe the microstructure, fracture morphology, cross-section morphology, and two-dimensional (2D) and 3D morphology of wear scratches. X-ray diffraction (XRD, X Pertpro) was used for coating phase identification. The compressive and tensile strength of the samples were measured by universal testing machine ETM 305D, stretching and compression rate is 5 mm/min and 2 mm/min, respectively. The wear tester MFT-4000 was used to measure the wear resistance, the ZrO_2 ceramic ball (HRC > 90) with 5 mm diameter is chosen as grinding ball. During experiments, the 1 kg weight is chosen as the applied load, the reciprocating stroke is 5 mm, the wear speed is 200 mm/min, and the wear time is 100 min. The microhardness tester EM500-2A was employed to measure the microhardness of the samples, applying 500gf load to hold 10 s.

Results and discussion

Quality and structure analysis of cladding layer

Cross-section morphology

Figure 3 shows the cross-section morphology of the samples under different overlap modes, the different overlap modes generate different remelting mode on the solidified layer, forming different metallurgical bonding zones. According to the Fig. 3(a–c), the scanning strategy directly determines the overlap area distribution and metallurgical band. Variation of overlap zone changes the temperature gradient and heat dissipation rate of the coating, affecting the microstructure characteristics. From the samples 1–3 and 1–4 (Fig. 3(a,d)), the overlap zone is directional. The distribution difference of overlap zone in layers fabricated by overlap modes 2 and 5 (Fig. 3(b, e) and Fig. 3(c,f)) in two directions is gradually reduced. The remelting area of the solidified layers and the temperature input becomes uniform, which minimizes microstructure differences and reduces the internal defects.[15] No macro-cracks appeared in all samples, indicating that the coating prepared with optimized process parameters had good metallurgical bonding quality, and the content of elements of the small black spot in the cladding layer is oxides of silicon (according to the Fig. 5). Noteworthy, the black spots mainly appear in the overlap area. The micro-melt particles oxidized to form oxides. The remelting temperatures in the overlapped areas failed to melt these oxides, resulting in a small black defect in the overlap area.

XRD analysis

Figure 4 shows the X-ray diffraction patterns of samples 1–4 and 5–4. The diffraction peaks of $Cr_{0.19}Fe_{0.7}Ni_{0.11}$, [Fe, Ni], Ni–Cr–Nb–Mo are detected in the samples. The change of temperature gradient caused the difference of diffraction peak intensity.[23] The overlap mode only changes the remelting mode and temperature distribution, improves the metallurgical bonding quality between layers and clad tracks. The composition of the coating remains unchanged, and no new phase is detected. The temperature distribution generated by the overlap mode affects crystallization and recrystallization transition as well as crystal orientation. In the sample 5–4, the remelting

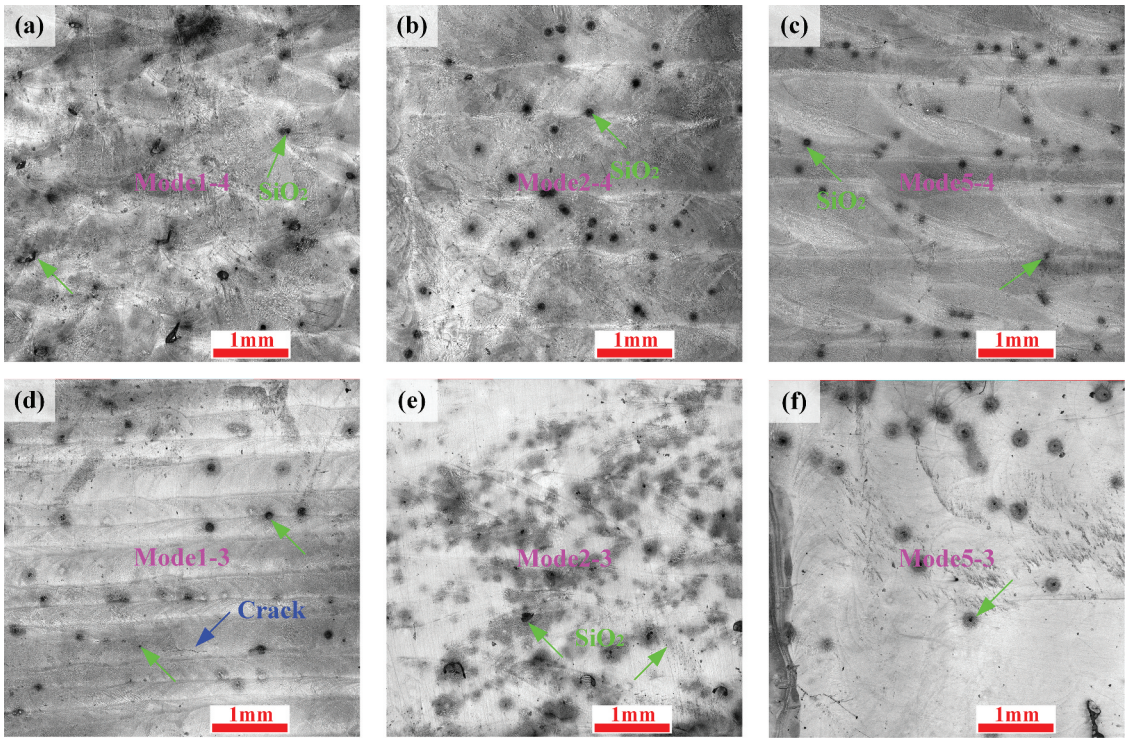

Figure 3. Cross-section morphology of different overlap modes. (a) Sample 1–4, (b) Sample 2–4, (c) Sample 5–4, (d) Sample 1–3, (e) Sample 2–3, (f) Sample 5–3.

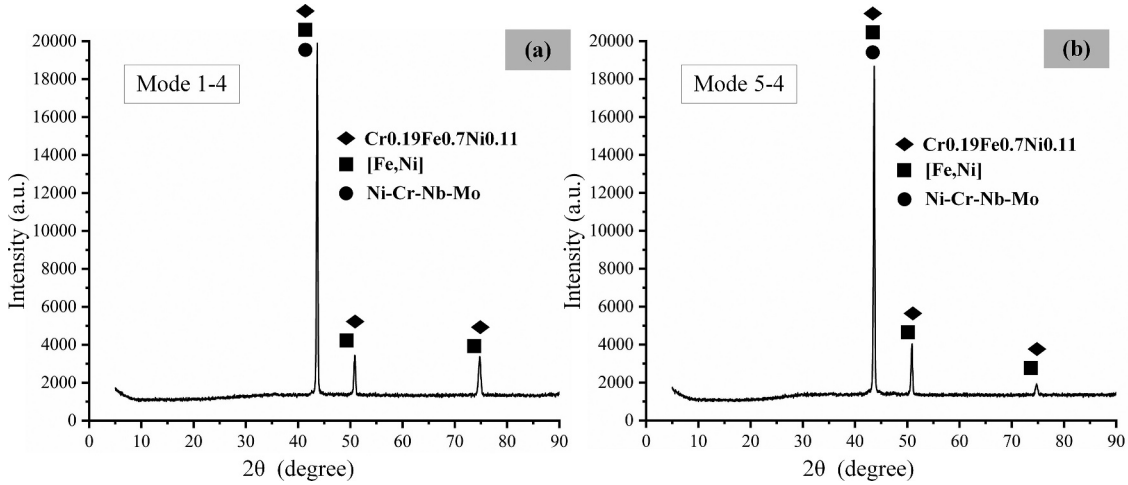

Figure 4. XRD patterns of Ni204-based cladding layers. (a) Sample 1–4; (b) Sample 5–4.

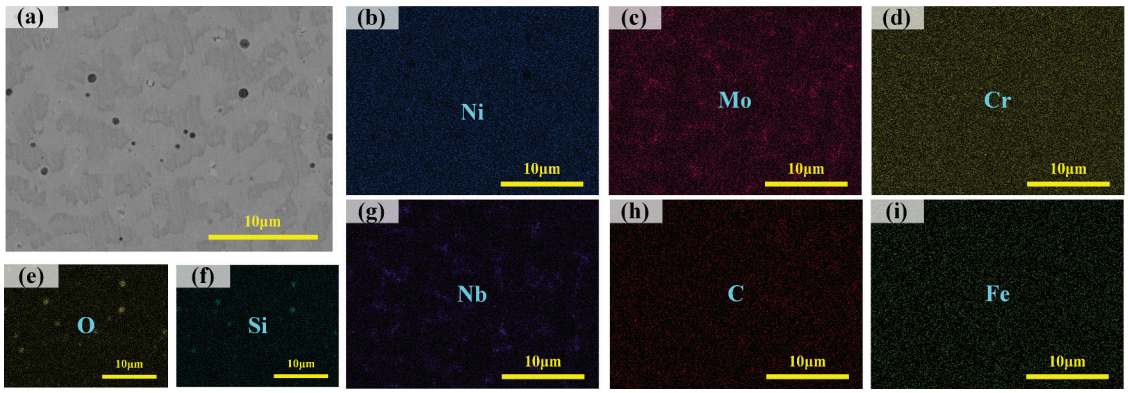

Figure 5. EDS maps showing the distribution of Ni, Mo, Cr, Nb, C, Fe, Si, O in sample 1–4.

of overlap area and the temperature distribution is more uniform, and the cooling rate is low, decreasing the preferential growth trend of grain along a crystal plane.[16]

Microstructure analysis

The EDS mapping of spatial distribution of Ni, Mo, Cr, Nb, C, Fe, Si and O in samples 1–4 is shown in Fig. 5. Figure 5(b–d) and (g) reveal that the gray phase on grain boundaries mainly contains Ni, Cr, Nb and Mo. Combing with Fig. 6, the milky white phase mainly composes of Nb and Mo. According to the XRD test results, Ni–Cr–Nb–Mo is identified the main phase in the grain boundaries. The Ni, Cr, Fe, Nb, and Mo elements first form multiple liquid phases. As the liquid phase solidifies, the second phase [Nb, Mo] and oxides precipitated,[22,24] existing in the Ni–Cr–Nb–Mo grain boundary. The Cr, Fe, and Ni mainly appear in the intracellular to form $Cr_{0.19}Fe_{0.7}Ni_{0.11}$ phase[25] and [Fe, Ni] solid solution. Si as a slag element, and finally in the form of oxides with other metal elements precipitate in the grain boundary (Fig. 5(e,f)).

The EDS line scan distribution of Mo, Nb, Ni, Cr, and Fe in the sample 2–4 is presented in Fig. 6. One can find that the content of Nb and Mo increases rapidly and Ni decreases at the precipitated phase boundaries. Figures 4 and Figures 5 reveal that the precipitated phase in grain boundaries is [Nb, Mo]. The eutectic components are precipitated firstly due to the low solid solubility when the grains grow up, and the [Nb, Mo] phase is pushed out at the grain boundary, forming the discontinuous substances. The [Nb, Mo] segregation affects the performance uniformity and plasticity of the coating, and increases the thermal cracking tendency. The secondary phase [Nb, Mo] is related to the thermal strength of the coating,[26] so the grain boundary segregation should be avoided as far as possible.

Figure 7 shows the SEM image (overlap area) and EDS spectrum of sample 5–4, the spectrum 1 (rectangular area) is dominated by Ni (59.93%) and 20.74% Cr, 8.94% Mo, 3.04% Nb, 1.16% Fe, and 0.45% Si are also detected, which is consistent with that of Ni204 powder, indicating no segregation generates in the overlap area. There is little difference in grain size between the overlap area and its two sides, and the overlap area primarily contains dendrite crystals.

Figure 8 demonstrates the microstructure at different magnifications for samples 5–4, 2–4, and 1–4, respectively. In Fig. 8 (a–c) (sample 1–4), the dendrite crystals mainly appear in the overlap areas and the difference of microstructure is the greatest. The scanning strategy of sample 1–4 generates single remelting mode, generates the difference temperature gradient and the uneven temperature distribution. Therefore, a large number of slender dendrites appear in the cladding layer. The fast fusion layer-cooling rate is not conducive to the

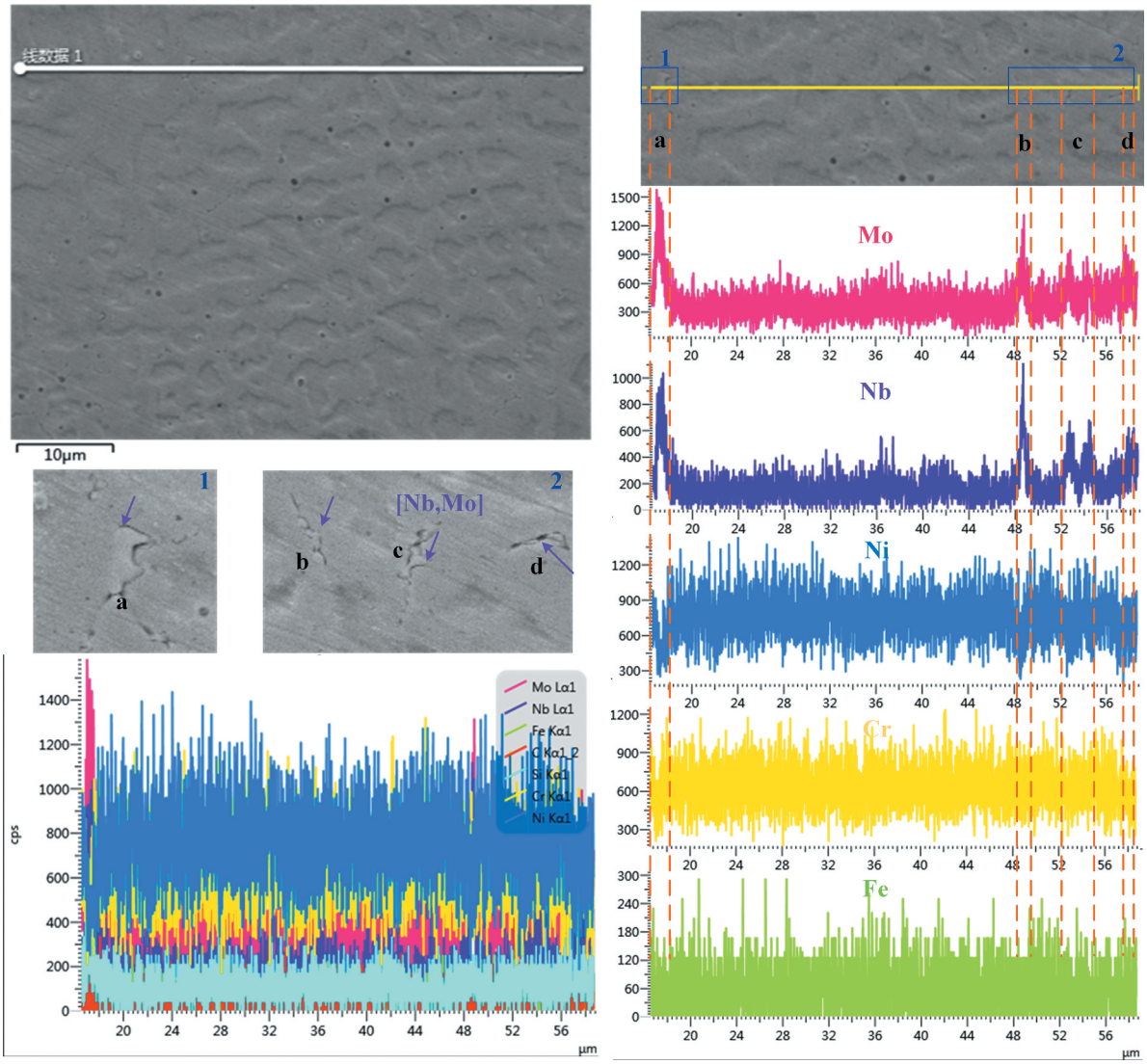

Figure 6. EDS line scan results of Ni, Mo, Cr, Nb, Fe in sample 2–4.

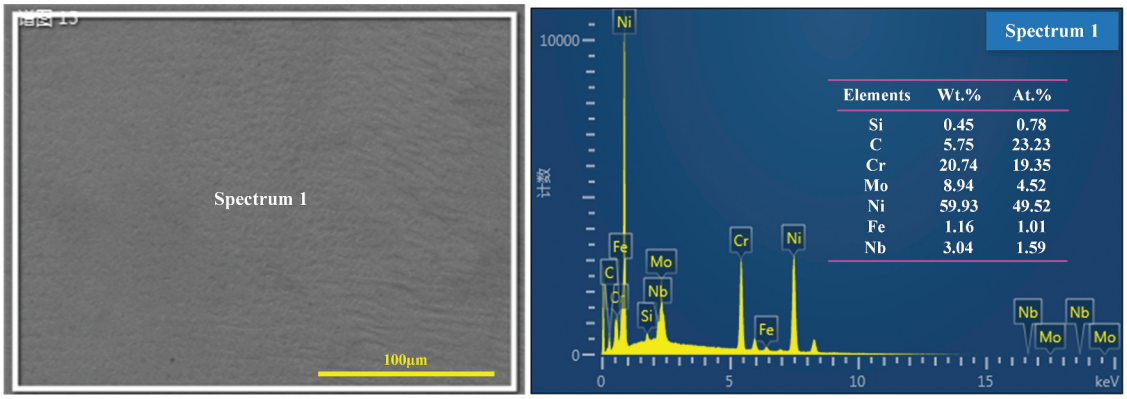

Figure 7. EDS spectra result in sample 5–4.

precipitation of the second phase [Nb, Mo], so the content of the second phase [Nb, Mo] in the grain boundaries is low. Compared with sample 1–4, the microstructure difference of sample 2–4 is decreased (Fig. 8(d–f)). The uniformity of remelting in solidification coating decreases the differences in grain growth time and nucleation rate, reducing difference in microstructure characteristics. The lower degree of sub-cooling increased the number of second-phase precipitation. In addition, the [Nb, Mo] phase in grain boundary changes from small pieces to discontinuous chains, increasing the incompleteness of grain boundaries. According to Fig. 8(g–i), the layer contains columnar, dendritic, equiaxed and cellular crystals, and

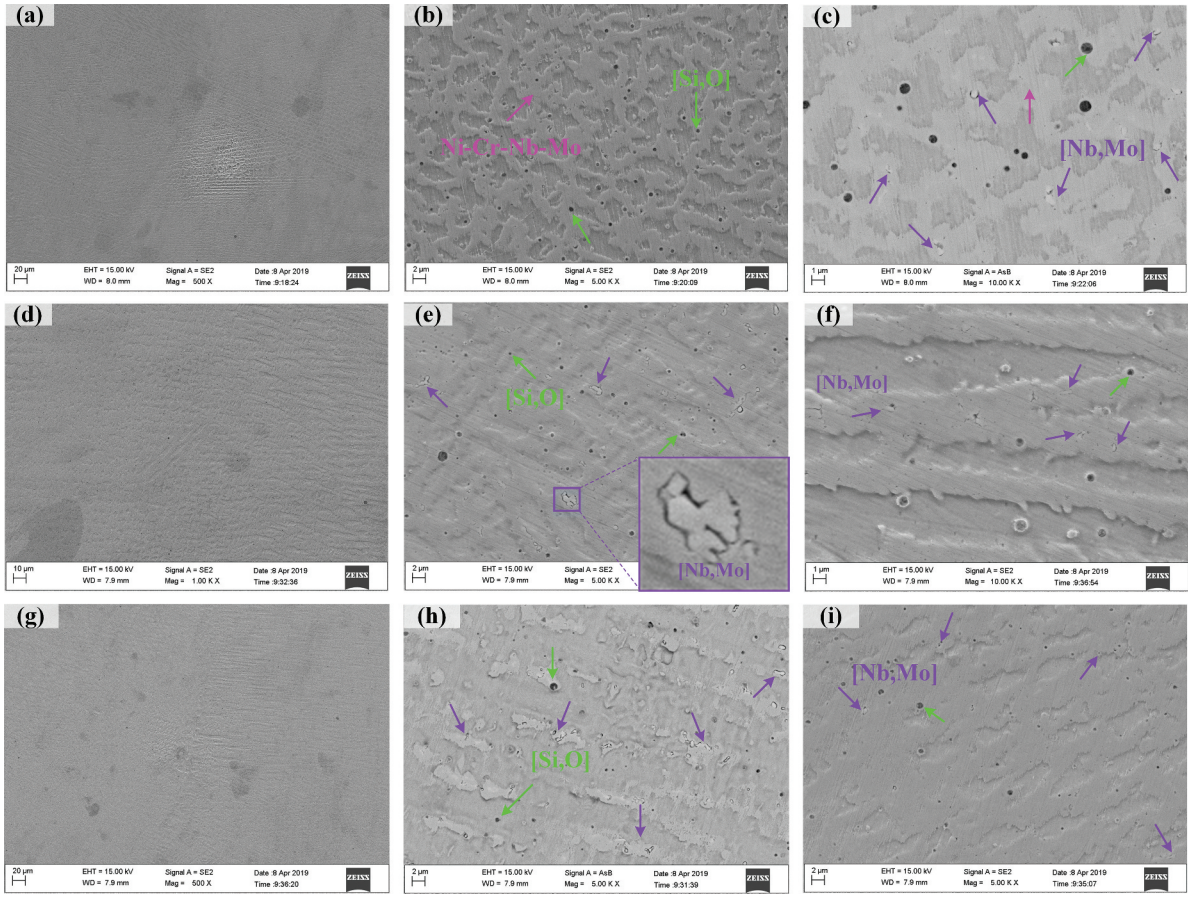

Figure 8. SEM images of samples. (a)–(c) Microstructures of sample 1–4; (a)–(c) Microstructures of sample 2–4; (a)–(c) Microstructures of sample 5–4.

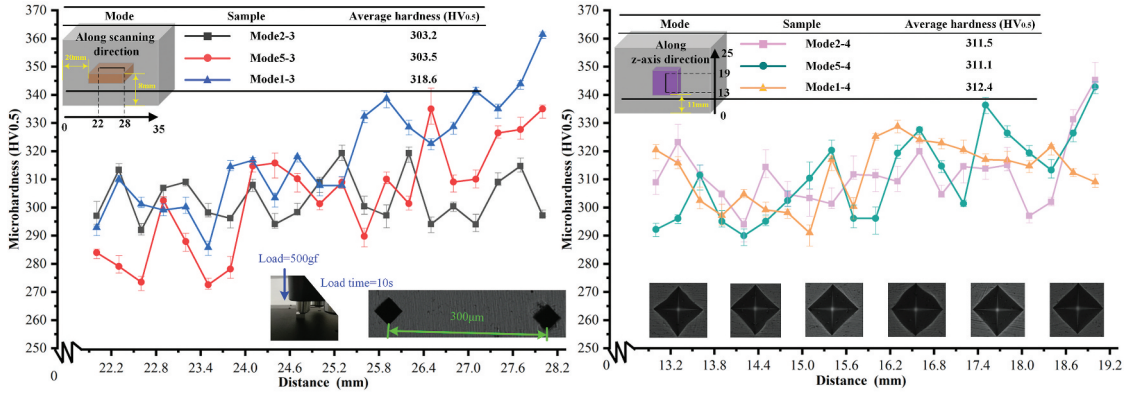

Figure 9. Microstructure of the samples.

the content and size of the second phases precipitated at the boundary are small. The sample 5–4 has a uniform remelting mode and longer growth time of grains. Owing to the remelting recrystallization and longer growth time in the overlap area, the columnar crystals continue to grow and undergo columnar dendrites. The small temperature gradient in the overlap area made the dendrite thicker, strengthened the convection in the coating, and promoted the dendrite fracture. Low cooling speed promotes the precipitation of the second phase,[26] the more locations of grain boundaries precipitate out [Nb, Mo], forming fine discontinuous chains. The precipitation of the second phase at the grain boundary can effectively refine the grain and stabilize the structure.[27] The layer-cooling rate and temperature are related to the overlap mode, causing different microstructure uniformity.

Microhardness and wear resistance measurement and analysis

Figure 9 shows the microhardness distribution of Ni204 cladding layer along the scanning direction and the Z-axis direction under different overlap modes. Spacing of adjacent test

points is 300 μm. The microhardness of samples 1–4, 2–4, and 5–4 prepared along z-axis direction are 312.4 $HV_{0.5}$, 311.1 $HV_{0.5}$, and 311.5 $HV_{0.5}$, respectively. The samples 1–3, 2–3, and 5–3 prepared along scanning direction are 318.6 $HV_{0.5}$, 303.2 $HV_{0.5}$, and 303.5 $HV_{0.5}$, respectively. Noteworthy, the microhardness fluctuates along scanning direction is larger than the direction along the z-axis, and the overlap mode presents a little effect on the microhardness.[28] The overlapped area along scanning direction is mainly composed of thick dendrites, while the inner part of the molten pool is mainly composed of dense isometric crystals. The difference in microstructure is primarily responsible for the hardness fluctuations. Along the Z-axis direction, the microstructure differences are reduced, so the microhardness distribution is more stable and larger than that in the horizontal direction.

The matrix is equivalent to a frame to bond the precipitate phase and hard phase together. Although the supporting capacity of the matrix affects the hardness of the coating, hard phase and precipitated phase play a leading role in resisting external deformation and enhancing the hardness of the coating.[16] The phase composition, microstructure characteristic, and precipitation phase at the grain boundary and in the intergranular have not changed under various scanning strategies. Compared with sample 5, the microhardness fluctuation of sample 2 is small in both directions. The discontinuous precipitation phase at the grain boundary is unfavorable to the microhardness of the coating. Therefore, the microstructure differences and discontinuous precipitated phase at the grain boundary both affect the coating hardness.

Figure 10 shows the friction coefficient curves of Ni204 cladded layers fabricated with different overlap modes. The experiments were carried out at room temperature. Compared with the sample prepared by overlap mode 5, overlap modes 1 and 2 oscillate larger in the two directions to varying degrees, mainly due to the influence of homogeneity of internal structure and defects. All the samples undergo surface damage, adaptive friction (lasted for 5 minutes), transition friction (ranges from 5 to 20 minutes), and plateau friction (after 20 minutes). When the wear time ranges from 5 to 20 minutes, the surface micro peak is ground off, the actual contact area increases, and the wear rate decreases. After 20 minutes, the coefficient of friction increases gradually. As the test continues, the contact area between the grinding ball and the sample increases. In addition, the big hardness difference between the ZrO_2 ball and the Ni204 layer generated a serious adhesive wear, increasing the friction coefficient. In the 60–80 min wear stage, the order of the friction coefficients of the samples is: 5–4 (μ = 0.655) < 2–3 (μ = 0.686) < 1–3 (μ = 0.718) < 1–4 (μ = 0.727) = 2–4 (μ = 0.727) < 5–3 (μ = 0.751). Sample 5–4 shows the minimum friction coefficient growth rate of 7.7% (friction coefficient at 60–80 min vs. initial stage) and has the minimum friction coefficient (μ = 0.64) in the whole testing process. The friction coefficients for each stage are given in Table 3.

The 2D and 3D morphologies of the wear surface are shown in Fig. 11, the obvious furrow wear scratches and chipping pits are observed, the laser-cladded Ni204 samples demonstrate adhesive and abrasive wear. In the wear testing experiment, the hard ZrO_2 ball directly scratches the surface of the Ni204 alloy layer, producing furrowed scratches on the surface. In addition, plastic deformation and shear failure occurs alternately on the surface of the sample, resulting in the soft Ni204 matrix sticking to the surface of the grinding ball. Meanwhile, the high friction temperature leads to the softening and adhesion of the metal at the contact point. According to Fig. 11(a-1–f-1), the sample that prepared by overlapped mode 5 has the best flatness of wear surface. Uniform microstructure distribution makes the wear surface have a high consistency in anti-deformation ability. The small plastic deformation difference in the wear area increases the evenness of the wear surface.

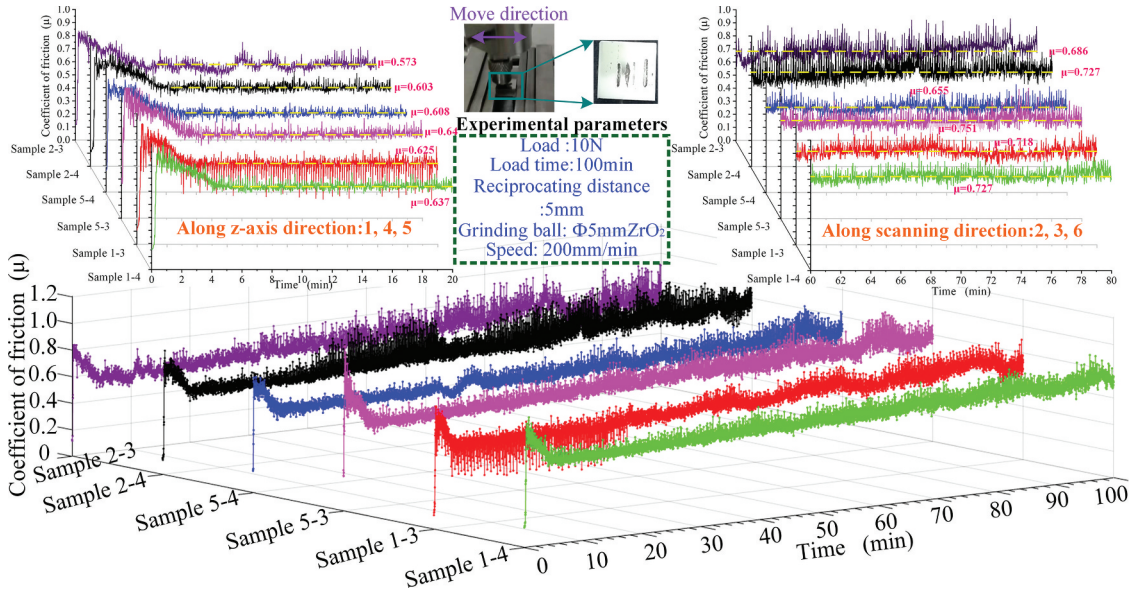

Figure 10. Coefficient of friction of the different specimens.

Table 3. Coefficient of friction in different time periods.

Specimen		Coefficient of friction (μ)				
Specimen preparation	No.	5–20 (min)	60–80 (min)	Growth rate (%)	5–100 (min)	Comment
Along z-axis direction	Sample 1–4	0.637	0.727	14.1	0.698	The friction coefficient of all specimens show an upward trend with the increase of time
	Sample 2–4	0.603	0.727	20.6	0.686	
	Sample 5–4	0.608	0.655	7.7	0.640	
Along scanning direction	Sample 1–3	0.625	0.718	14.9	0.679	
	Sample 2–3	0.573	0.686	19.7	0.640	
	Sample 5–3	0.64	0.751	17.3	0.716	

Strength measurement and analysis

Compressive strength measurement and analysis

Compressive strength test results for three overlap modes along z-axis direction and scanning direction are shown in Fig. 12. The samples are not crushed or fractured with the load increased, but is changed from a cylinder to a convex platform. No yield point and compression strength point appear on the stress-strain curve of all samples, indicating the Ni204 alloy presented good toughness. The samples fabricated with overlap modes 2 and 5 have stronger interlayer metallurgical bonding quality, better uniformity of microstructure distribution, and less tendency of shear stress during compression. Therefore, the compressive performance of overlap mode 1 is poor than overlap modes 2 and 5. When the strain is greater than 0.03, the elastic deformation of the sample disappears completely and enters the compaction and crushing stage. When compression deformation is between 0.01 and 0.03, one can find that the stress is different under the same deformation, which indicates that the overlap mode has an effect on the deformation resistance of the material. The order of deformation resistance is given by: sample 2–1 > sample 2–2 > sample 5–1 > sample 1–1 > sample 5–2 > sample 1–2. The yield limit of different overlap modes ranges from 550 to 600 MPa.

The overlap area has the coarse microstructure, the poor metallurgical bonding quality, and easily appeared defects.[16] The elongation direction of the overlap area and clad track of

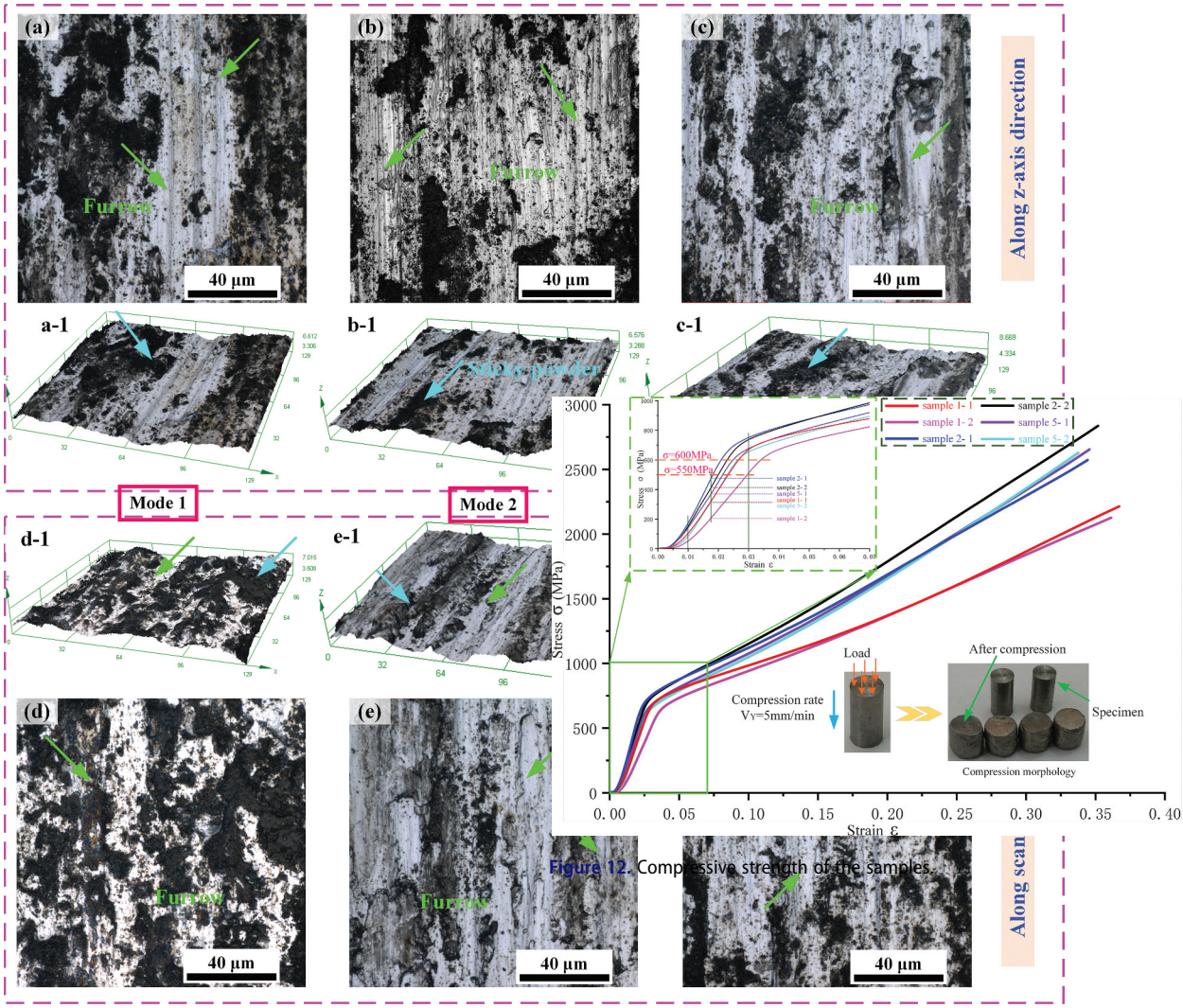

Figure 12. Compressive strength of the samples.

Figure 11. Wear surface morphology of the Ni204 specimens.

sample 1–2 is perpendicular to the direction of load, causing the overlap area is easier to be compacted, while the elongation direction of the overlap area of sample 1–1 is parallel to the direction of load. The microstructure difference in the coating makes the clad track bend and the overlap area compacted during the compression process. Therefore, the compressive stress of the sample is small under the same deformation. During compression of sample 5–2, the compaction of inter-laminar overlapped areas and the shear and compaction induced by the difference of the microstructure are reduced, improving the deformation resistance. In addition, the changing scanning direction reduces the anisotropic growth of the microstructure, improving the deformation resistance.[23] Therefore, the shear stress induced by non-uniformity of pressure and microstructure is not conducive to the improvement of deformation resistance. The angle between strategy direction of sample 5–1 and load direction is 90, 0, and 45 degrees. For sample 2–2 is 90 and 0 degrees. During compression, the clad tracks with 0 degrees hinder the compaction of the overlap area with 90 degrees. While the clad tracks with 90 degrees blocks the tear of the overlap area with 0 degrees. Thus the deformation resistance of the melt layer is improved. Sample 2–1 has the best anti-deformation ability. The strategy direction is perpendicular to the direction of load, and the overlap zone is regularly remelted. Therefore, the mutually perpendicular clad tracks play a certain role in enhancing the anti-deformation ability of each direction, thus improving the anti-deformation ability. Compared with overlap mode 2, overlap mode 5 has high uniformity of microstructure, but the direction of microstructure growth is also disordered. During compression, the regularity of shear force caused by the difference in microstructure is poor; moreover, the discontinuous precipitated chain phase [Nb, Mo] at grain boundary reduces the deformation resistance of the sample, so the deformation resistance of the sample fabricated by mode 5 is weaker than that of mode 2.

Tensile strength measurement and analysis

Figure 13 shows the tensile stress-strain curves of the samples under five different overlap modes. The results show that the overlap mode can effectively change the tensile strength of the laser-cladded Ni204 samples, and no yield process appears in the stretching process. The tensile strength of overlap mode 1 was the highest and the tensile strength is 886.9 MPa. The other overlap modes follow the given order: overlap mode 5 (848.3 MPa), overlap mode 4 (779 MPa), overlap mode 2 (777.9 MPa) and overlap mode 3 (752.3 MPa). The corresponding elongation is 34.2%, 33.9%, 21.2%, 25%, and 31.1%, respectively. For the overlap mode 1 ('long straight' scanning strategy), the elongation direction of overlap zone is parallel to the direction of tensile force. The ductility and strength of the clad tracks are conformable in the tensile direction without considering the shear stress caused by the difference in microstructure. The sample is equivalent to screw the clad tracks together and only subjected to tensile stress during stretching. Therefore, the sample fabricated by overlap mode 1 has the highest tensile strength and the maximum elongation when the failure occurs. The metallurgical bonding zone generated by the overlap mode 5 ('double vertical cross') is disorderly. The uniform remelting improves the strength of the interlayer metallurgical bonding, reduces the difference in microstructure and the internal defects, and improves the coating strength. Although the overlapped mode 5 introduced shear force in the process of stretching, different interlayer overlapped modes have hindered the generation of partial shear. Overcoming shear forces are mainly responsible for the lower tensile strength than overlap mode 1. The scanning strategy of overlap mode 4 is 'short straight'. The metallurgical bonding direction is perpendicular to the tensile stress. The coarse grains in the overlap area cause the overlap area to be broken first during stretching, showing poor elongation. It can be seen that the metallurgical bonding quality of the overlapped area plays a decisive role in the ductility of the sample. In overlap mode 2 ('vertical cross'), the angle between the elongation direction of overlap area and stress alternates between 0 degrees and 90 degrees. The overlap area (90 degrees) is not conducive to tensile strength and ductility, but the overlap area in the direction of 0 degrees prevents the overlap area in the direction of 90 degrees from being pulled apart, improving the ductility and tensile strength of the sample. In addition, the different deformation resistance in two directions generated shear stress, causing the sample tearing. In overlap mode 3 ('oblique vertical cross'), the angle between direction of overlap zone and tensile stress is 45 degrees. The overlapped mode improves the strength of the inter-laminar metallurgical bond. Therefore, the elongation direction of overlap mode 3 is greater than that of overlap mode 2. However, this overlap mode introduces the greatest shear force, the most severe tear generated during stretching, and its tensile strength is the lowest. According to the stretching morphology, the fracture line of the sample fabricated by overlap mode 3 is the most sloping, while the fracture line of overlap modes 1 and 4 is horizontal. The dip angle of the fracture line is closely related to the angle between the elongation direction of overlap zone and the applied load, as well as to the shear stress caused by the difference in microstructure and uneven force.

Significant differences in mechanical behavior can be found from tension (Fig. 12) and compression (Fig. 13) testing. Although the alloy showed a yield strength of 550–600 Mpa in tension and compression, the deformation resistance was

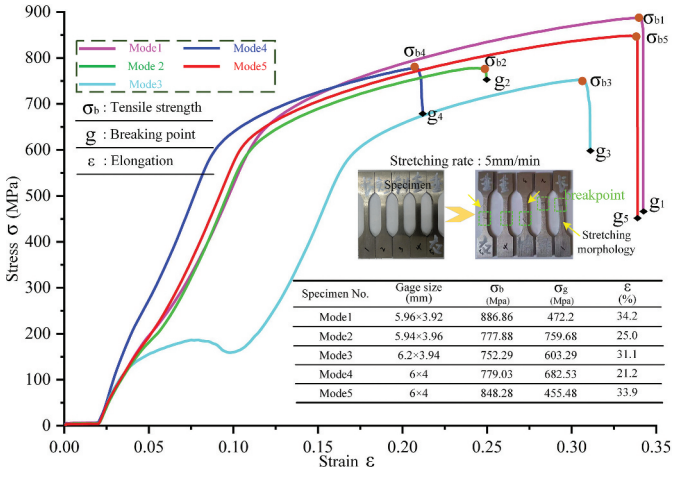

Figure 13. Tensile strength of the specimen.

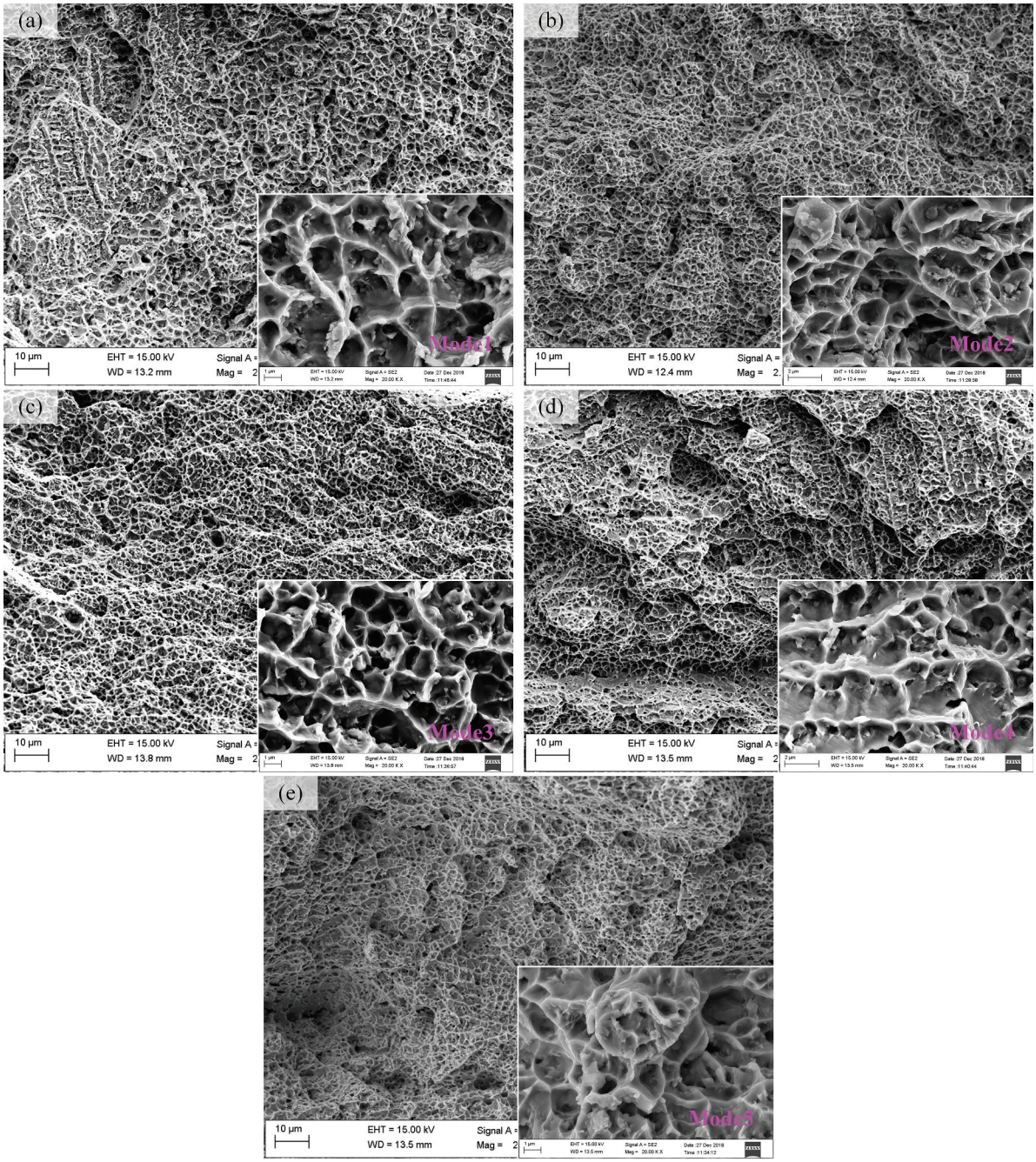

Figure 14. Fracture morphology of the tensile specimens. (a) Overlap mode 1, (b) Overlap mode 2, (c) Overlap mode 3, (d) Overlap mode 4, (e) Overlap mode 5.

markedly different in the different overlap mode. The samples exhibited continuous compaction and sustained work hardening during compression, and no crushing or failure before the end of the test. However, in tension, the Ni204 alloy demonstrated limited work hardening. All samples failed after the true strain of 0.35. The grain boundary cracks reduce the flow stress and result in the sample failure.[29] Although the uniformity of the layer microstructure is improved by changing the overlap mode, the angle between the strategy direction and applied loading generates shear stress, which is unfavorable to the tensile and compressive strength. The high strength of the inter-laminar metallurgical bonding improves the shear deformation of the samples.

Figure 14 shows the SEM images of the tensile fracture morphology, the dimples on the fracture surface are much and deep. Ductile fracture via the micro-voids growth and coalescence mechanism is the dominant fracture mode. During the tensile process, the obvious necking phenomenon was observed. The plastic deformation of the tensile sample produces micro-voids, and then nucleate, grow, aggregate, and finally connect with each other, resulting in fracture and dimple formation.

Conclusions

Multi-cladding layers were fabricated using Ni204-based alloy as a deposited material under different overlap modes. By

investigating the layer properties, the anisotropy of mechanical behavior of coating is a direct result of laser manufacturing technology. The overlap mode has great influence on the preferred orientation of grain.

The matrix is mainly composed of $Cr_{0.19}Fe_{0.7}Ni_{0.11}$, [Fe, Ni], Ni–Cr–Nb–Mo, and [Nb, Mo]. The second phase [Nb, Mo] precipitated from the grain boundary Ni–Cr–Nb–Mo. The uniformity distribution of scanning trajectory on the cladding plane reduces the difference of microstructure and promotes the precipitation of [Nb, Mo] at grain boundary. The average value of microhardness of different overlap modes is between 303.2 $HV_{0.5}$ to 318.6 $HV_{0.5}$, the friction coefficient is between 0.64 and 0.716. By improving the microstructure uniform, the stability of microhardness and friction coefficient distribution are improved, but not obvious for the strengthening effect on the properties. Grain size is the primary factor affecting stability of microhardness. Ni204 exhibits the abrasive wear and adhesive wear. The tensile and compression properties of different overlap modes are quite similar, ranges from 550 to 600 Mpa, but big difference after yield. The performance is directly determined by the angle between the strategy direction and the applied loading. The overlap mode 1 has the highest tensile strength (886.86 MPa) which is higher 1.18 times than the smallest overlap mode 3 (752.29 MPa).

Funding

This work was supported by the Fundamental Research Funds for the Central Universities [N180306004]; The Ministry of Industry and Information Technology of China under Grant [No. 201675514]; The Science and Technology Planning Project of Shenyang under Grant [No.18006001].

References

[1] Chen, Y.; Guo, Y.; Lu, B.; Xu, M.; Xu, J. Microstructure and Properties of the Interface Area in the Laser Cladded Ni Based Coatings on the 1Cr10Mo1NiWVNbN Steel. *Metals*. 2017, *7*(175), 1–9. DOI: 10.3390/met7050175.

[2] Chamanfar, A.; Jahazi, M.; Cormier, J. A. Review on Inertia and Linear Friction Welding of Ni-Based Superalloys. *Metall. Mater. Trans. A*. 2015, *46*, 1639–1669. DOI: 10.1007/s11661-015-2752-4.

[3] Zeng, C.; Tian, W.; He, W.; Hua, L. Microstructure and Porosity Evaluation in Laser-cladding Deposited Ni-based Coatings. *Surf. Coat. Technol.* 2016, *294*, 122–130. DOI: 10.1016/j.surfcoat.2016.03.083.

[4] Vilar, R.; Almeida, A. Repair and Manufacturing of Single Crystal Ni-based Superalloys Components by Laser Repair and Manufacturing of Single Crystal Ni-based Superalloys Components by Laser Powder Deposition — A Review. *J. Laser Appl.* 2016, *27*, S17004. DOI: 10.2351/1.4862697.

[5] Wang, X.; Deng, D.; Qi, M.; Zhang, H. Influences of Deposition Strategies and Oblique Angle on Properties of AISI316L Stainless Steel Oblique Thin-walled Part by Direct Laser Fabrication. *Opt. Laser Technol.* 2016, *80*, 138–144. DOI: 10.1016/j.optlastec.2016.01.002.

[6] Shu, D.; Li, Z.; Zhang, K.; Yao, C.; Li, D.; Dai, Z. In Situ Synthesized High Volume Fraction WC Reinforced Ni-based Coating by Laser Cladding. *Mater. Lett.* 2017, *195*, 178–181. DOI: 10.1016/j.matlet.2017.02.076.

[7] Liu, H.; Hu, Z.; Qin, X.; Wang, Y.; Zhang, J. Parameter Optimization and Experimental Study of the Sprocket Repairing Using Laser Cladding. *Int. J. Adv. Manuf. Technol.* 2017, *91*, 3967–3975. DOI: 10.1007/s00170-017-0066-y.

[8] Naghiyan, M.; Shoja-razavi, R.; Allah, H.; Jamali, H. Microstructure Investigation of Inconel 625 Coating Obtained by Laser Cladding and TIG Cladding Methods. *Surf. Coat. Technol.* 2018, *353*, 25–31. DOI: 10.1016/j.surfcoat.2018.08.061.

[9] Qian, D.; Zhang, A.; Zhu, J.; Li, Y.; Zhu, W.; Qi, B.; Tamura, N.; Li, D.; Chen, K. Hardness and Microstructural Inhomogeneity at the Epitaxial Interface of Laser 3D-printed Ni-based Superalloy. *Appl. Phys. Lett.* 2016, *109*(10), 101907. DOI: 10.1063/1.4962485.

[10] Teomete, E.; Dimas, L. S.; Buehler, M. J. Study on Pores and Crack Sensitivity of Ni- Based Composite Coating by Laser Cladding Study on Pores and Crack Sensitivity of Ni-based Composite Coating by Laser Cladding. *PCM 2015* 2015, *87*, 012096. DOI: 10.1088/1757-899X/87/1/012096.

[11] Wen, P.; Cai, Z.; Feng, Z.; Wang, G. Microstructure and Mechanical Properties of Hot Wire Laser Clad Layers for Repairing Precipitation Hardening Martensitic Stainless Steel. *Opt. Laser Technol.* 2015, *75*, 207–213. DOI: 10.1016/j.optlastec.2015.07.014.

[12] Li, Y.; Chen, K.; Tamura, N. Mechanism of Heat Affected Zone Cracking in Ni-based Superalloy DZ125L Fabricated by Laser 3D Printing Technique. *Mater. Des.* 2018, *150*, 171–181. DOI: 10.1016/j.matdes.2018.04.032.

[13] Yu, T.; Zhao, Y.; Sun, J.; Chen, Y.; Qu, W. Process Parameters Optimization and Mechanical Properties of Forming Parts by Direct Laser Fabrication of YCF101 Alloy. *J. Mater. Process. Technol.* 2018, *262*, 75–84. DOI: 10.1016/j.jmatprotec.2018.06.023.

[14] Zhao, Y.; Yu, T.; Sun, J.; Xi, W.; Bi, X. Effect of Laser Cladding on Forming Qualities of YCF101 Alloy Powder in the Different Lap Joint Modes. *Int. J. Adv. Manuf. Technol.* 2018, *96*, 1991–2001. DOI: 10.1007/s00170-018-1732-4.

[15] Ren, K.; Chew, Y.; Fuh, J. Y. H.; Zhang, Y. F.; Bi, G. J. Thermo-mechanical Analyses for Optimized Path Planning in Laser Aided Additive Manufacturing Processes. *Mater. Des.* 2019, *162*, 80–93. DOI: 10.1016/j.matdes.2018.11.014.

[16] Paydas, H.; Mertens, A.; Carrus, R.; Lecomte-beckers, J.; Tchuindjang, J. T. Laser Cladding as Repair Technology for Ti–6Al–4V Alloy : Influence of Building Strategy on Microstructure and Hardness. *Mater. Des.* 2015, *85*, 497–510. DOI: 10.1016/j.matdes.2015.07.03.

[17] Li, Y. X.; Ma, J. Study on Overlapping in the Laser Cladding Process. *Surf. Coat. Technol.* 1997, *90*, 1–5. DOI: 10.1016/s0257-8972(96)03022-8.

[18] Calleja, A.; Tabernero, I.; Fernández, A.; Celaya, A.; Lamikiz, A.; López De Lacalle, L. N. Improvement of Strategies and Parameters for Multi-axis Laser Cladding Operations. *Opt. Lasers Eng.* 2014, *56*, 113–120. DOI: 10.1016/j.optlaseng.2013.12.017.

[19] Yi, P.; Liu, Y.; Shi, Y.; Jang, H. Investigation on the Process of Laser Surface Melting Using Two Sequential Scans. *Int. J. Adv. Manuf. Technol.* 2011, *57*, 225–233. DOI: 10.1007/s00170-011-3270-1.

[20] Petrat, T.; Winterkorn, R.; Graf, B.; Gumenyuk, A.; Rethmeier, M. Build-up Strategies for Temperature Control Using Laser Metal Deposition for Additive Manufacturing. *Weld. World* 2018, *62*, 1073–1081. DOI: 10.1007/s40194-018-0604-8.

[21] Zhao, Y.; Yu, T.; Wang, Z.; Chen, H. Calculation and Verification of Start/Stop Optimum Overlapping Rate on Metal DLF Technology. *Int. J. Adv. Manuf. Technol.* 2018, *99*, 437–452. DOI: 10.1007/s00170-018-2445-4.

[22] Zhao, Y.; Yu, T.; Guan, C.; Sun, J.; Tan, X. Microstructure and Friction Coefficient of Ceramic (Tic, TiN and B_4C) Reinforced Ni-based Coating by Laser Cladding. *Ceram. Int.* 2019, *45*, 20824–20836. DOI: 10.1016/j.ceramint.2019.07.070.

[23] Li, K.; Li, D.; Liu, D.; Pei, G.; Sun, L. Microstructure Evolution and Mechanical Properties of Multiple-layer Laser Cladding Coating of 308L Stainless Steel. *Appl. Surf. Sci.* 2015, *340*, 143–150. DOI: 10.1016/j.apsusc.2015.02.171.

[24] Jang, J. Y.; Shim, H.; Lee, Y. J.; Lee, S. H.; Lee, J. G. Application of Negative Pressure Wound Therapy in Patients with Wound Dehiscence after Abdominal Open Surgery: A Single Center

Experience. *J. Korean Surg. Soc.* 2013, *85*, 180–184. DOI: 10.4174/jkss.2013.85.4.180.

[25] Liu, Y.; Xu, T. H.; Liu, Y.; Gao, Y. L.; Di, C. Wear and Heat Shock Resistance of Ni-WC Coating on Mould Copper Plate Fabricated by Laser. *J. Mater. Res. Technol.* 2020, *9*, 8283–8288. DOI: 10.1016/j.jmrt.2020.05.083.

[26] Liu, J.; Tian, C. Influence of Second Phase on the Mechanism of Interaction between Fatigue and Creep for GH33A. *Acta Aeronautica et Astronautica Sinica (China)* 1989, *7*, A404–A408.

[27] Fensin, S. J.; Jones, D. R.; Walker, E. K.; Farrow, A.; Imhoff, S. D.; Clarke, K.; Trujillo, C. P.; Martinez, D. T.; Gray, G. T.; Cerreta, E. K. The Effect of Distribution of Second Phase on Dynamic Damage. *J. Appl. Phys.* 2016, *120*, 085901. DOI: 10.1063/1.4961041.

[28] Zhang, Z.; Kovacevic, R. A Thermo-mechanical Model for Simulating the Temperature and Stress Distribution during Laser Cladding Process. *Int. J. Adv. Manuf. Technol.* 2019, *102*, 457–472. DOI: 10.1007/s00170-018-3127-y.

[29] Joseph, J.; Stanford, N.; Hodgson, P.; Fabijanic, D. M. Tension/compression Asymmetry in Additive Manufactured Face Centered Cubic High Entropy Alloy. *Scr. Mater.* 2017, *129*, 30–34. DOI: 10.1016/j.scriptamat.2016.10.023.